

# Origin of transverse ridges on the surfaces of catastrophic mass flow deposits on the Earth and Mars

S. M. Baloga

Proxemy Research, Bowie, Maryland, USA

B. C. Bruno

Hawai'i Institute of Geophysics and Planetology, University of Hawai'i, Honolulu, Hawaii, USA

Received 16 November 2004; revised 11 February 2005; accepted 14 March 2005; published 21 May 2005.

[1] Transverse ridges on the surfaces of catastrophic mass flow deposits such as landslides, debris flows, and lahars may be the remnants of surface waves that originated during transit. Such waves can form as a result of a flow instability or from irregularities or pulses in the release of material at the source. We first consider a steady state release of material into the flow. By considering classic fluid dynamic stability criteria, we show that flow instabilities known to lead to roll waves seem likely for the mass flow deposits studied on Earth and Mars. Motivated by the plausibility of dynamic wave formation, we consider the more realistic case of a time-dependent release of material into the flow by performing a detailed mathematical analysis of the momentum and volume conservation equations. The results show that for some regimes of flow conditions, any disturbances in the source conditions grow downstream without bound, much like a classical fluid dynamic instability. It is conjectured that this regime may lead to analogs of roll waves. In other regimes, however, any irregularities in the boundary conditions at the source of the flow decay, as in a stable fluid flow. One critical parameter delineating the regimes of stability and instability is the time constant for the decay of the flow depth at the source. When surface waves are preserved in the deposits of long runout, catastrophic mass flows, our results provide a new diagnostic for constraining the emplacement conditions and the rheology of the flow during transit.

**Citation:** Baloga, S. M., and B. C. Bruno (2005), Origin of transverse ridges on the surfaces of catastrophic mass flow deposits on the Earth and Mars, *J. Geophys. Res.*, *110*, E05007, doi:10.1029/2004JE002381.

## 1. Introduction

[2] Surface waves, pulses and time-dependent effects are common in mass flows of geologic interest, such as debris flows, landslides, lahars and lava flows. In dense mass flows such as the Elm [Heim, 1882, 1932] and Blackhawk [Shreve, 1968] landslides, the Chaos Jumbles [Eppler *et al.* 1987; Bulmer *et al.*, 2002b, 2002c, 2003] and numerous lava flows, wave structures are preserved on the flow surface (Figure 1). They have also been observed as transients in debris flows and rapidly moving fluid lava flows [Moore, 1987; Iverson, 1997; Lipman and Banks, 1987].

[3] Geologists sometimes think of waves on the surface of a mass flow as the result solely of the cessation of flow front advance and an accommodation of the surface upstream. They sometimes ignore the possibility that surface waves and wave-like features can result from flows that are turbulent or internally disrupted. Yet, regularly spaced, steadily propagating water waves are common on windowpanes, driveways and streams during periods of heavy rainfall. Surface waves result naturally from the

dynamics of such flows whenever there is an excess flow rate above that which can be accommodated as a stable steady state. Such waves originate while the flow is in motion due to basic momentum and volume conservation considerations. Their existence and shape are unrelated to the cessation of flow advance.

[4] Wave structures on surface flows of water dissipate as the flows thin or slow. But, for dense mass flows, the action of intergranular forces can preserve a record of the waves that existed while the flow was in motion. In the case of rapidly emplaced lava flows, the cooling of the surficial crust often preserves surface waves, pulses and transients. For less dense mass flows (e.g., low-density debris flows, lahars or hyper-concentrated water flows), a record of the existence of waves may persist in the residual sediment deposits.

[5] We investigate two dynamical origins for surface wave formation on catastrophically released mass flows during flow advance. One mode of formation is similar to a fluid dynamic instability, whereas the other results from pulses, variations or irregularities in conditions at the source of the mass flow. Both these origins are dynamical: they are associated fundamentally with the time-dependent equations that govern momentum and volume conservation while the

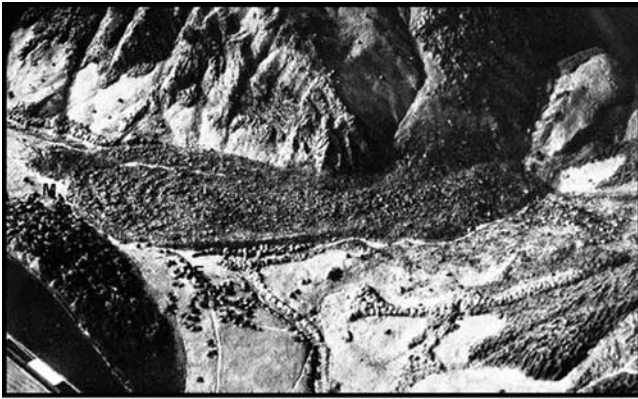


**Figure 1.** Elm, Switzerland, 1881 landslide with prominent surface waves preserved in the distal deposit (courtesy of Julio Friedmann).

flow is in transit. We base our approach on the classic stability analysis of a steady flow of water with uniform depth in a rectangular channel on an inclined plane [Jeffreys, 1925]. More elegant treatments of this classic analysis have become part of the standard literature of stability analysis [Chow, 1973; Whitam, 1974], but the original theoretical and empirical results remain valid today.

[6] Our primary theoretical extension is to treat the catastrophic mass flow release as a pulse-like, time-dependent boundary condition instead of as a steady state with a constant depth. Analogous to Jeffreys [1925], we determine the flow conditions that cause waves to form and grow, versus those that dissipate small perturbations in the boundary conditions at the source of the flow.

[7] In this work, we will often refer to “the source of the flow.” In actuality, landslides, debris flows and lahars can be released catastrophically from broad areas, from multiple locations, and according to a variety of scenarios and time sequences. For modeling purposes, however, it is assumed here that any sources of mass flux eventually become consolidated into a single, continuously fed, coherent flowing unit. This location is taken as  $x = 0$  and the behaviors of the flow thickness and velocity at this point along the flow path are used to define the boundary conditions. We do not consider any of the detailed possible mechanics of the release of material (e.g., slope failures or seismic fracturing), but take the formation of a single, coherent flowing unit as a given.

[8] First, we consider the plausibility of surface wave formation of a dynamical origin for some large terrestrial and Martian landslides with surface features suggestive of waves. To determine whether a dynamic origin is plausible, we initially use Jeffreys’ [1925] stability criteria and some estimates of flow conditions derived by a variety of means. We investigate the Elm and Blackhawk landslides, Chaos Jumbles and the ridged deposits in the plains to the northwest of Arsia and Pavonis Montes in the Tharsis region of Mars. We have selected the Elm and Blackhawk landslides because the surfaces of the deposits have wave-like structures and they have been studied extensively in the literature. Many of the details of emplacement for the Chaos Jumbles are presently ambiguous and await further field study [Bulmer et al., 2002b]. However, the waves preserved

on the surfaces of these deposits are more complicated structures than the simple sinusoidal waves that one might expect (Figure 2). Figure 3 shows a MOC image of a prominent ridged deposit northwest of Arsia Mons. Similar deposits are found northwest of Pavonis Mons. While a host of alternative genetic possibilities is cited by Head and Marchant [2003], here we consider the possibility that the ridged deposit in Figure 3 was formed by one or more landslides off the northwest flank of the volcano.

[9] In section 2, we review the key ideas in a conventional stability analysis of a steady fluid flow of uniform depth and velocity on an inclined plane. Then, in section 3, using various dimensional and velocity data from the literature, we apply the steady state stability criteria to the examples above to see if the formation of surface waves during transit would be anticipated. Even with the uncertainties in the details of emplacement, we find a strong suggestion that waves might form in all of the terrestrial and Martian examples.

[10] This indication of surface wave formation in the steady state motivates our theoretical investigation of the more realistic case of a time-dependent release of material at the source of the flow (sections 4–6). We investigate how surface waves might form on large mass flows as a result of basic momentum and volume conservation dynamics. We obtain mathematical criteria for the unconstrained growth of perturbations in the boundary conditions. These criteria are analogous to stability criteria in that they delineate the regime of flow parameters that preserves the overall behavior of the source conditions as they propagate downstream. In the text, we provide only a summary of the mathematical analysis and the key results. The details of the derivations are provided in Appendix A. We find that the time dependence in the boundary conditions produces an unexpectedly rich variety of surface waves that may be recorded in the deposits of landslides, debris flows and lahars. This mechanism may also be responsible for the surges in large basaltic lava flows [Lipman and Banks, 1987; Moore, 1987] and perhaps many of the regular wave-like surface structures often seen on distal segments of lobate basaltic and basaltic andesite lava flows.

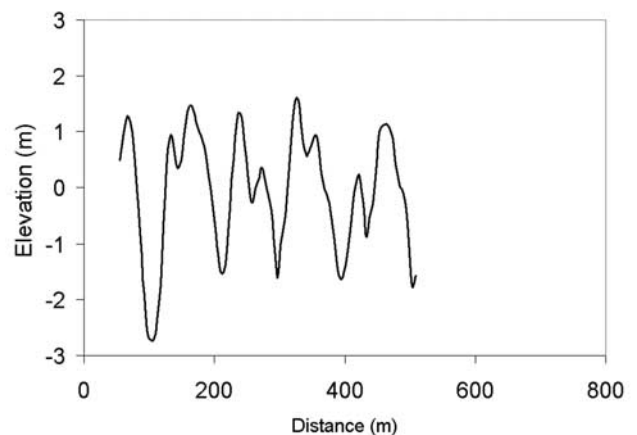


**Figure 2.** Complex surface waves on Chaos Jumbles deposit. Overall topographic gradient has been removed [Bulmer et al., 2002b].

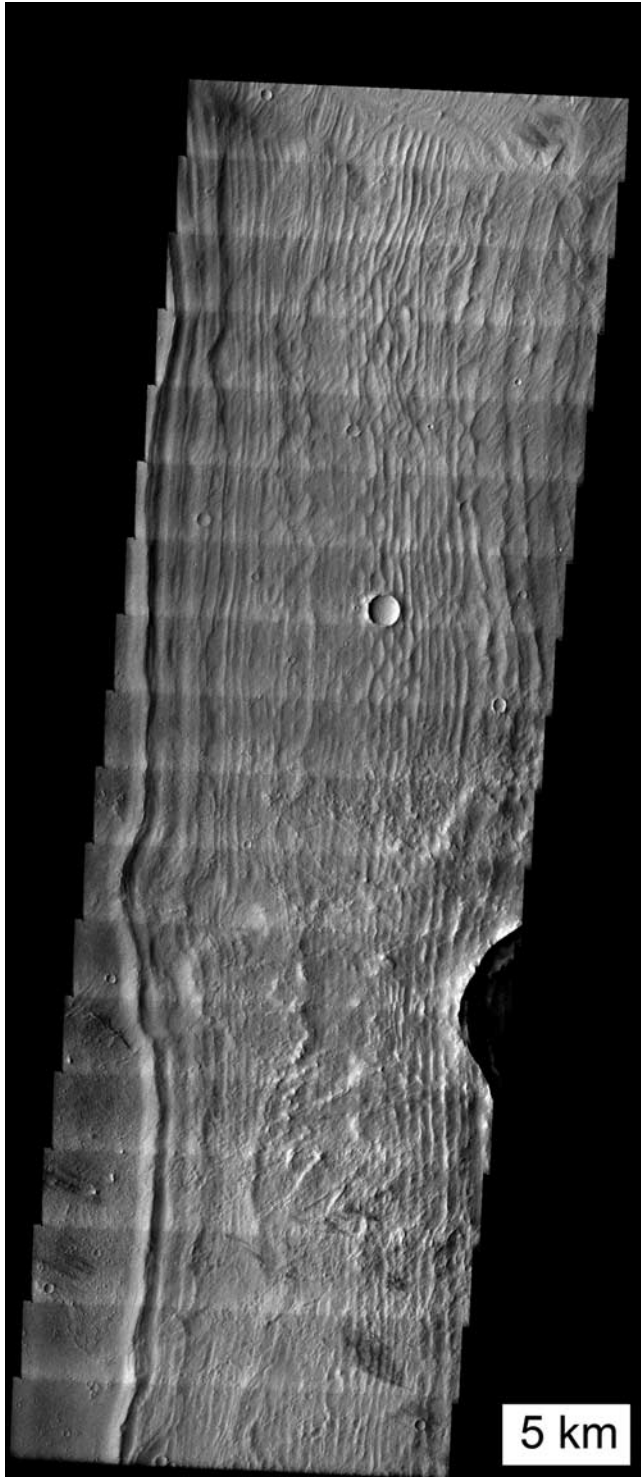


**Figure 3.** Ridged deposit on the NW flank of Arsia Mons. Image resolution is 18 m/pixel and image center is 5.0°S, 229.6°E (THEMIS visible image V01703002).

[11] In section 7, we apply our results to the ridged deposits on the plains northwest of Arsia and Pavonis Montes. We do not attempt to argue that such ridged deposits are the result of catastrophic mass flows off the flanks of these volcanoes. Possible modes of formation of these deposits have been debated in the literature for many years and some are unrelated to catastrophic mass flows

(see *Head and Marchant* [2003] for a concise review and related references.) The arguments for and against various alternative origins of the ridged deposits deal with issues (e.g., morphologic diagnostics) other than those addressed in this work. However, if these deposits were the result of rapidly emplaced mass flows, the existence of waveforms and our theoretical results combine to provide new constraints on the details of emplacement and the bulk rheology of the material.

## 2. Review of Steady State Stability Analysis

[12] The classic approach to determining the conditions for the stability of a steady water flow in a channel is based on the volume and momentum conservation equations:

Volume conservation

$$\frac{\partial h}{\partial t} + \frac{\partial}{\partial x}(hu) = 0, \quad (1)$$

Momentum conservation

$$\frac{\partial u}{\partial t} + u \frac{\partial u}{\partial x} = g \sin \theta - Cu^2/h - g \cos \theta \frac{\partial h}{\partial x}. \quad (2)$$

[13] Table 1 provides the definitions of the mathematical symbols used in this work. In (2), the terms on the left-hand side represent inertia. The terms on the right-hand side represent gravity and frictional resistance to flow and pressure, respectively. In the steady state, all the derivatives in (1) and (2) are zero, and the solutions  $h(x, t) = h_0$  and  $u(x, t) = u_0 = \sqrt{g \sin \theta h_0 / C}$  are constants. The flow resistance parameter,  $C$ , has been estimated in the literature for many types of rapidly emplaced mass flows in various settings. Values range from 0.0025 for water in a channel to approximately unity for dense debris flows [e.g., *Takahashi*, 1980; *Weir*, 1982; *Baloga et al.*, 1995; *Bulmer et al.*, 2002a; *Glaze et al.*, 2002].

**Table 1.** Mathematical Symbols

Symbol	Definition	Unit <sup>a</sup>
$x$	downstream distance	m
$t$	time	s
$l$	flow length	m
$w$	flow width (constant)	m
$h$	flow depth	m
$\Delta e$	elevation climbed	m
$u$	flow velocity	m/s
$\tau$	time parameter	–
$Q_0$	volumetric flow rate (constant)	m <sup>3</sup> /s
$g$	gravitational acceleration	m/s <sup>2</sup>
$\theta$	slope	deg
$C$	coefficient of flow resistance	–
$\eta$	perturbation in flow depth	–
$\eta_0$	perturbation in flow depth at the source	–
$\xi$	perturbation in flow velocity	–
$h_R$	flow depth (reference solution)	m
$h_0$	initial flow depth (constant)	m
$u_R$	flow velocity (reference solution)	m/s
$u_0$	initial flow velocity (constant)	m/s
$L$	length scale	m
$\Gamma$	decay constant of flow depth	s
$T$	duration of the mass release	s
$P$	period of the oscillation in the depth perturbation	s
$\varepsilon$	inertial parameter	–
$\kappa$	pressure gradient parameter	–

<sup>a</sup>A dash (“–”) in units column indicates a dimensionless quantity.

**Table 2.** Steady State Stability Analysis of Elm and Blackhawk Landslide Deposits

	$l$ , km	$w$ , km	$h$ , m	$\Delta e$ , m	$\theta$ , °	$C_{crit}$	$u$ , m/s	$C$	Waves Expected?	Ridges Observed?
Elm <sup>a,b</sup>	1.4	.5	18.3	104	2–4	0.009–0.018	45.1	0.003–0.006	yes	yes
Blackhawk <sup>a</sup>	8	2.4	15.2	60	3	0.013	34.3	0.007	yes	yes

<sup>a</sup>Shreve [1968].

<sup>b</sup>Heim [1882, 1932]. Dimensional data are estimates and in some cases measured from topographic maps included in the literature. All units were converted to metric.

[14] To determine whether the steady state is stable or not, small sinusoidal spatial perturbations of uniform flow depth and velocity along the flow path are introduced. Small inhomogeneities or irregularities are always present in natural situations due to variations in topography, the confining perimeter of the flow and/or the density or rheology of the flowing medium itself. Two new governing equations for the perturbations are generated from (1) and (2). They describe to first-order the influence of the derivatives neglected in a uniform flow. For some sets of flow parameters, the assumed small perturbations in the flow depth and velocity will decay with time to the original uniform steady state. For this regime of flow parameters, the flow is said to be stable. For other sets of flow parameters, however, the initially small perturbations will grow in time without bound. Under these conditions, the flow is said to be unstable.

[15] The specific conditions for a stable steady state of depth  $h_o$  and velocity  $u_o$  take the simple equivalent forms

$$\tan \theta \leq 4C, \quad (3)$$

$$u_o \leq 2\sqrt{\cos \theta g h_o}, \quad (4)$$

$$Q_o = u_o h_o w \leq 2h_o w \sqrt{\cos \theta g h_o}. \quad (5)$$

When any of these conditions are not met, the uniform flow becomes unstable. Small perturbations in the flow depth and velocity profiles grow with time and these profiles transition to more complicated forms. A conventional stability analysis by itself cannot determine the ultimate form of the growing perturbations. It can only indicate that a transition from the reference state will occur. Additional mathematical or experimental analysis must be performed to determine whether periodic waves will form on the flow surface and, if so, the character of the waveform. In the case of water flows in natural and fabricated channels, it is known empirically and analytically that regularly spaced, stable roll waves form on the flow surface [Cornish, 1910; Jeffreys, 1925; Dressler, 1949; Whitham, 1974; Townson, 1991; Carver *et al.*, 1994]. Roll waves are known in hydrology as “bores”; that is, they are steadily propagating discontinuous mathematical solutions of (1) and (2). There are no continuous periodic traveling wave solutions of (1) and (2). For this reason, the shape of roll wave profiles was not determined until Dressler’s [1949] work. Illustrations are given by, for example, Whitham [1974, and references therein]. For our purposes, it is sufficient to know that roll waves form a sequence of regularly spaced segments with an almost monoclinal growth in amplitude and a very sharp front at the end of each segment. In the subsequent sections,

we will suggest that formation of roll waves could be the cause of the wave-like features on the deposits of some catastrophic mass flows.

### 3. Application to Steady State Mass Flows

[16] We now apply the above steady state stability criteria (equations (3)–(5)) to three classic examples of landslides with long runout distances: 1881 Elm landslide (Elm, Switzerland), Blackhawk landslide (Lucerne Valley, California) and the Chaos Jumbles (Lassen Volcanic National Park, California). All three deposits show well-developed wave structures, oriented transverse to the presumed flow direction. Their existence suggests that flow conditions were unstable and that waves (possibly analogs of roll waves) formed on the surface during transit.

[17] From (3), we find that a hypothetical steady state mass flow is unstable when  $C$  is less than the critical value:

$$C_{crit} = \frac{\tan \theta}{4}. \quad (6)$$

For  $C < C_{crit}$ , we would expect to find evidence of a wave pattern that might be preserved on the surface. Additionally,  $C$  would generally be expected to exceed 0.0025 (i.e., be less fluid than water). Thus the critical range of  $C$  for unstable flows is

$$0.0025 < C < \frac{\tan \theta}{4}. \quad (7)$$

[18] Solving the steady state form of (2), we obtain

$$C = \frac{g \sin \theta h}{u^2}. \quad (8)$$

[19] From (8), we estimate  $C$  for the three mass flow examples from data, observations and inferences regarding the thickness, velocity and topographic slope. Subsequently we determine whether the estimated  $C$  lies within the critical range given by (7). Our results are summarized in Tables 2 (Elm and Blackhawk landslides) and 3 (Chaos Jumbles).

#### 3.1. Elm and Blackhawk

[20] For deposits that were emplaced essentially as a single coherent unit (such as the Elm and Blackhawk landslides), we estimate  $h$  and  $u$  as follows. For  $h$ , we use the average thickness of the final flow deposit. We acknowledge that this is simply an approximation of the dynamic flow thickness (e.g., the flow may have thickened during the cessation of flow advance). We calculate  $u$  by assuming the elevation climb was accomplished solely by converting kinetic to potential energy:

$$u = \sqrt{2g \Delta e}. \quad (9)$$

**Table 3.** Steady State Stability Analysis of the Chaos Jumbles Deposit (Phases I–III)

	$l^a$ , km	$w^a$ , km	$h^a$ , m	$\theta^a$ , °	$C_{crit}$	$u_{min}^b$ , m/s	$u_{max}^b$ , m/s	$u^a$ Estimates	Ridges Observed? <sup>a</sup>
Phase I	4.5	1.5	8.2	2	0.009	17.6	33.5	0–68	yes
				6	0.026	18.0	58.0	68–79	
Phase II	3.5	1.4	13.7	2	0.009	22.8	43.3	0–23	yes
				6	0.026	23.2	74.9	23–55	
Phase III	2	0.8	12.9	6	0.026	22.4	72.7	0–97	yes

<sup>a</sup>*Eppler et al.* [1987]. Dimensional data are estimates and in some cases measured from topographic maps included in the literature.

<sup>b</sup>Minimum and maximum velocities expected to produce surface waves.

[21] Our results are shown in Table 2. In the one case (Elm) where eyewitness accounts are available, our velocity estimate of 45.1 m/s corresponds well with eyewitness reports of 110 miles/hour (49 m/s) [*Heim*, 1882, 1932]. Finally, ambient slopes vary across the long runout distances of these deposits. Thus we calculate not a single value but a range of  $C$  based on the range of slope values found in the literature. For both Elm and Blackhawk, the calculated  $C$  values are less than  $C_{crit}$  yet greater than 0.0025, indicating from (7) that dynamical instabilities would be expected to develop in transit. This is consistent with the observed wave structures remaining on the deposit surface.

### 3.2. Chaos Jumbles

[22] The Chaos Jumbles was emplaced by collapse of the Chaos Crags dacite dome complex. Unlike the Elm and Blackhawk deposits, it was not emplaced as a single unit. Instead, it appears to have been emplaced in three separate phases [*Shreve*, 1968], each composed of multiple layers [*Bulmer et al.*, 2003]. Thus the total elevation surmounted by the landslide is not likely to yield a meaningful estimate of flow velocities by the simple kinetic-to-potential energy conversion given by (9).

[23] We can however determine what range of velocities would correspond to the critical range of  $C$  and evaluate these values for reasonableness (Table 3). For comparison, velocity estimates based on *Heim*'s [1932] kinematic analysis are also listed in Table 3 [*Eppler et al.*, 1987]. Their analysis is predicated on two key assumptions: (1) the dome that collapsed was at least as high as the highest point of the breakaway scar, and (2) the original prelandslide topography had a similar slope and morphology to the present topography.

[24] From (7) and (8), the velocities required for instabilities to form range from 17.6 to 74.9 m/s (39–168 miles/hour) for the three phases of the Chaos Jumbles. These values seem quite reasonable on the basis of intuitive considerations. In contrast, some of *Eppler et al.*'s [1987] values appear unrealistically high (97 m/s = 217 miles/hour), which may suggest a reexamination of one or more of their assumptions. Nevertheless, in four of the five cases, the two ranges of velocity estimates (at least somewhat) overlap, suggesting the *Jeffreys*' [1925] stability criteria is a reasonable way of estimating flow velocities when the deposits contain evidence of waves during transit.

### 3.3. Arsia and Pavonis Montes, Mars

[25] We now turn our attention to the transverse ridged flow surfaces in the plains northwest of the Martian Tharsis volcanoes Arsia and Pavonis Montes. Among the origins proposed to explain these surface ridges are lahars, debris flows, pyroclastic flows and glacial deposits [*Head and*

*Marchant*, 2003, and references therein]. On the basis of MOLA data, *Head and Marchant* [2003] estimate individual inner ridge heights at Arsia as 5–20 m, with the outer prominent ridge as  $\sim$ 50 m high. For Pavonis Mons, *Shean and Head* [2003] similarly estimate inner ridge heights as 5–30 m, with the outer ridge reaching 50–100 m high.

[26] Here, we consider the possibility that these ridges represent the distal portions of a lahar or debris flow using the approach outlined above for the Chaos Jumbles deposit. Any such flow would likely have originated on the relatively steep upper flanks of the volcanoes, estimated as approaching 3° from flank profiles derived from MOLA data [*Morris et al.*, 2003]. Again, these slope values are input into (7) to determine the critical range of  $C$ . The next step is to determine the range of flow velocities that would correspond to this critical range of  $C$  from (8) based on  $h$  and the Martian value for gravitational acceleration (3.74 m/s<sup>2</sup>). As dynamic flow depth  $h$  during transit is unknown, we consider a range of values on the order of the measured ridge heights (10, 20, 50m). These results are presented in Table 4.

[27] The velocities required for instabilities to form on these deposits range from 12.2 to 62.5 m/s (27–140 miles/hour). These velocities are very plausible and are on the order of those determined for the three terrestrial deposits studied. Thus, on the sole basis of fluid dynamic considerations, there is no inconsistency in the hypothesis that the ridges formed as the result of an instability. Conversely, as argued in section 7, if one assumes an initial velocity within this range, surface waves would be anticipated.

## 4. Time-Dependent Reference Solution

[28] The classical reference solution used for a stability analysis is obtained by assuming that the gravitational and frictional terms balance in (2), all other terms in the momentum equation are negligible, and the flow depth and velocity are constant at the source of the flow. In this

**Table 4.** Steady State Stability Analysis of Arsia and Pavonis Montes Ridged Flows

$\theta$ , °	$C_{crit}$	$h^{a,b}$ , m	$u_{min}^c$ , m/s	$u_{max}^c$ , m/s	Ridges Observed? <sup>a,b,d</sup>
3	0.013	10	12.2	27.9	yes
3	0.013	20	17.3	39.5	yes
3	0.013	50	27.3	62.5	yes

<sup>a</sup>*Head and Marchant* [2003].

<sup>b</sup>*Shean and Head* [2003].

<sup>c</sup>Minimum and maximum velocities expected to produce surface waves.

<sup>d</sup>*Morris et al.* [2003].

work, we retain the first two assumptions, but allow the flow depth and velocity to change with time at the source of the flow. Following previous models of lahars and debris flows [Weir, 1982; Glaze *et al.*, 2002; Fagents and Baloga, 2004], we use the time-dependent boundary condition at the source for flow depth,

$$h(x=0, t) = \frac{h_o}{(1+t/\Gamma)^2}, \quad (10)$$

and the resulting time-dependent velocity boundary condition,

$$u(x=0, t) = \frac{u_o}{(1+t/\Gamma)}. \quad (11)$$

[29] These boundary conditions make the flow depth and velocity start at maximum values  $h_o$  and  $u_o$  at the source ( $x=0$ ) and at the onset ( $t=0$ ) of the mass flow. Subsequently, the depth and velocity decay monotonically with a rate determined by the time constant  $\Gamma$ . For a given  $g$ ,  $\theta$  and  $C$ , the initial velocity  $u_o$  is computed from

$$u_o = \sqrt{\frac{gh_o \sin \theta}{C}}. \quad (12)$$

[30] To find the time-dependent reference solutions, we neglect the influence of inertia and pressure in (1) and (2) and balance the gravitational and frictional forces at all downstream locations along the flow path. The resulting time-dependent flow thickness and velocity profiles are given [Glaze *et al.*, 2002; Fagents and Baloga, 2004] by

$$h_r(x, t) = h_o \left( \frac{1+x/L}{1+t/\Gamma} \right)^2 \quad (13)$$

and

$$u_r(x, t) = u_o \left( \frac{1+x/L}{1+t/\Gamma} \right), \quad (14)$$

where the length scale  $L$  is defined as

$$L = \frac{3\Gamma u_o}{2}. \quad (15)$$

## 5. Approximate Solution by Perturbation Analysis

[31] The inertial and pressure terms neglected to obtain (13) and (14) are identically the terms that determine whether a flow is stable or unstable. Now, we reintroduce the inertial and pressure gradient terms and determine how they would change (13) and (14) by the method of perturbations [Whitham, 1974; Zauderer, 1983]. Here we summarize the methodology detailed in Appendix A and present the key results.

[32] First, we make the volume and momentum conservation equations (1) and (2), the boundary conditions (10)

and (11), and the reference solutions (13) and (14) all dimensionless using the natural scaling factors

$$h = h_o h^*, \quad (16)$$

$$x = Lx^*, \quad (17)$$

$$t = \Gamma t^*, \quad (18)$$

$$u = u_o u^*, \quad (19)$$

where asterisks denote dimensionless terms. With these scalings, the volume and momentum conservation equations become

$$\frac{\partial h^*}{\partial t^*} + \frac{2}{3} \left( h^* \frac{\partial u^*}{\partial x^*} + u^* \frac{\partial h^*}{\partial x^*} \right) = 0 \quad (20)$$

and

$$\varepsilon \left( \frac{\partial u^*}{\partial t^*} + \frac{2}{3} u^* \frac{\partial u^*}{\partial x^*} + \kappa \frac{\partial h^*}{\partial x^*} \right) = 1 - \frac{u^{*2}}{h^*}, \quad (21)$$

respectively, where the two dimensionless parameters are defined as

$$\varepsilon = \frac{1}{\Gamma} \sqrt{\frac{h_o}{Cg \sin \theta}} = \frac{u_o}{\Gamma g \sin \theta} = \frac{3u_o^2}{2gL \sin \theta} \quad (22)$$

and

$$\kappa = \frac{2C \cot \theta}{3}. \quad (23)$$

[33] These two dimensionless parameters let us evaluate the competition between the stabilizing and destabilizing influences of pressure and inertia on the time-dependent reference solution. The parameter  $\varepsilon$  provides a measure of the influence of the inertial term in (21). As the influence of the inertial term increases, the flow tends to become unstable. The second dimensionless parameter  $\kappa$  gauges the influence of the pressure gradient in (21). This term tends to diminish any spatial gradients in the flow depth profile that may evolve in time. As  $\varepsilon$  and  $\kappa$  decrease, the flow tends to become more stable and vice versa.

[34] Equations (20) and (21) are a formidable nonlinear system of equations. Our approach is to use a linear perturbation expansion of the dimensionless flow depth and velocity:

$$h^* = h_R^* + \varepsilon \eta + O(\varepsilon^2), \quad (24)$$

$$u^* = u_R^* + \varepsilon \xi + O(\varepsilon^2), \quad (25)$$

where  $O(\varepsilon^2)$  indicates other terms that are at least quadratic in  $\varepsilon$ .

[35] The parameter  $\varepsilon$  is formed by the physical parameters  $h_o$ ,  $u_o$ ,  $g$ ,  $\theta$  and  $C$ , all of which are determined by nature for a particular mass flow event. Thus this method is only applicable to mass flows that make  $\varepsilon$  sufficiently small.

[36] To use the method of perturbations, (24) and (25) are substituted into (20) and (21). Only terms having prefactors with  $\varepsilon$  to either the zeroth or first power are retained. Any terms in the governing equations that have a prefactor of  $\varepsilon^2$  or higher are considered negligible. Thus our solutions for the corrected flow depth and velocity are said to be valid “to first order in  $\varepsilon$ .” Additional mathematical analysis would be required to find solutions to higher powers of  $\varepsilon$ .

[37] To first order in  $\varepsilon$ , it is shown in Appendix A that (24) and (25) make (20) and (21) reduce to a single equation:

$$\frac{\partial \eta}{\partial t^*} + \frac{(1+x^*)}{(1+t^*)} \frac{\partial \eta}{\partial x^*} + \frac{\eta}{(1+t^*)} + \left(\frac{4}{9} - \frac{8}{3}\kappa\right) \frac{(1+x^*)^3}{(1+t^*)^5} = 0, \quad (26)$$

and an algebraic relationship between the perturbed flow velocity and flow depth:

$$\xi = \frac{\eta}{2} \frac{(1+t^*)}{(1+x^*)} + \left(\frac{1}{6} - \kappa\right) \frac{(1+x^*)^2}{(1+t^*)^3}. \quad (27)$$

[38] The beauty of this perturbation approach is that we are left with a first-order partial differential equation (26) that can be readily solved by standard methods. The drawback is that the solution is valid only for  $\varepsilon$  sufficiently small that quadratic terms can be neglected.

[39] The general solution of (26) is derived in Appendix A as

$$\eta(x^*, t^*) = \frac{\eta_0(\tau)}{(1+x^*)} - \left(\frac{4}{9} - \frac{8}{3}\kappa\right) \frac{(1+x^*)^3 \ln(1+x^*)}{(1+t^*)^4}, \quad (28)$$

where

$$\tau = \tau(x^*, t^*) = \frac{1+t^*}{1+x^*} - 1 \quad (29)$$

and  $\eta_0(t^*) = \eta(x^* = 0, t^*)$  is the boundary value function that describes the behavior of the perturbation of the flow depth with time at the source.

[40] Equations (27)–(29) are the main results of our theoretical analysis. Once  $\eta_0(t^*)$  is prescribed, (28) is a general solution that tracks the behavior of the perturbed flow surface with time and downstream distance. In addition, we obtain the correction to the flow velocity as a function of time and downstream distance from (27).

[41] By inspection of (28), it is evident that any time-dependent variations in the flow depth at the source of the mass flow (i.e.,  $\eta_0(t^*)$ ) will be damped with distance by the  $(1+x^*)$  term. This behavior will be amplified or diminished by the term that arises from the pressure term containing  $\kappa$ . Interestingly, the separation of the boundary value and pressure terms in (28) suggests there may be flow regimes where all influence of the boundary value behavior may be lost. This would be analogous to a conventional stability

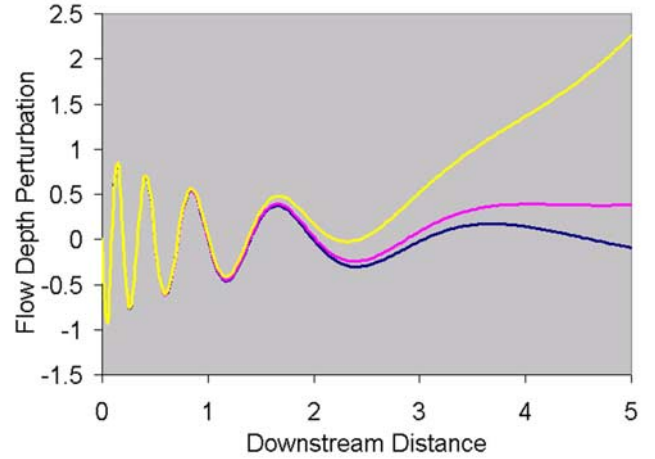


**Figure 4.** Plot of flow depth perturbation ( $\eta$ ) as a function of downstream distance ( $x^*$ ) for  $P^* = 1$ . Both axes are dimensionless. Three different  $\kappa$  values are shown: 0.05 (bottom curve), 0.65 (middle curve), and 3 (top curve). In all cases the amplitude of source oscillations damp within about 3 or 4 length scales, but the  $\kappa = 3$  curve grows without bound.

analysis in that the flow depth could evolve to a state that bears no resemblance to the reference solution (i.e., like an instability). Alternatively, the perturbed flow surface could revert to the original reference solution like a stable but time-dependent flow regime.

[42] When  $\kappa = 1/6$ , the perturbed flow surface given by (28) depends only on what happens at the source (i.e.,  $\eta_0(t^*)$ ). The large bracket term containing  $\kappa$  on the right-hand side of (28) vanishes. This special point corresponds identically to  $C \cot \theta = 1/4$ , the critical stability value for the steady state.

## 6. Results

[43] As discussed earlier, the conventional stability analysis of the uniform steady state is based on a sinusoidal spatial perturbation of the initial conditions. By analogy, we use a time-dependent boundary condition of the form

$$\eta_0(t^*) = \sin(2\pi t^*/P^*) \quad (30)$$

to analyze representative implications of (28). The argument for using such a form is that any arbitrary boundary condition can be constructed by Fourier methods from a superposition of periods [Kreyszig, 1988]. Equation (30) specifies small changes in the perturbed flow depth at the source that oscillate through a full cycle with a period  $P^*$ . It has been implicitly assumed that such oscillations occur at the source with a period  $P$ . The period has been made dimensionless by dividing  $P$  by the decay constant  $\Gamma$ . Numerical examples discussed below will help clarify these relationships.

[44] We now investigate what happens to such oscillations as they propagate downstream. In all examples, we assume that  $\varepsilon$  is sufficiently small so that our perturbation approach is valid, at least near the source. The two key parameters that we now vary are  $\kappa$  and  $P^*$ .

[45] Figure 4 shows the form of the surface waves for three representative  $\kappa$  values (0.05, 0.65, and 3) with  $P^* = 1$ .

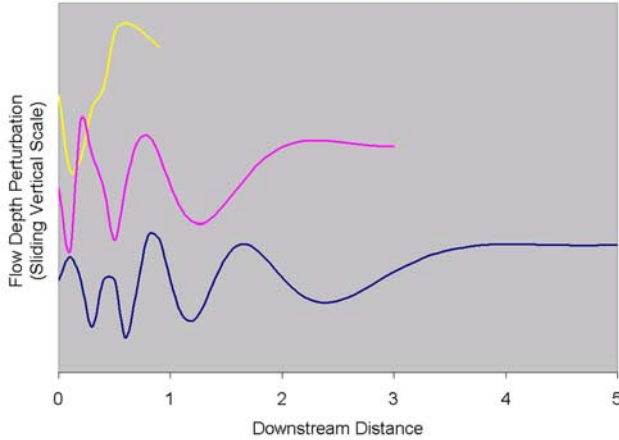


**Figure 5.** Plot of flow depth perturbation ( $\eta$ ) as a function of downstream distance ( $x^*$ ) for  $P^* = 1$ . Both axes are dimensionless. Snapshots at three dimensionless times ( $t^*$ ) are shown: 1 (top curve), 3 (middle curve), and 5 (bottom curve). Vertical scales have been offset for visual clarity.

In physical dimensions,  $P^* = 1$  means the oscillation period at the source is equal to the decay constant of the reference solutions. Significant conclusions are immediately evident from Figure 4. As expected, the amplitude of any oscillations at the source damps within about 3 or 4 length scales. A more subtle feature is that, for all values of  $\kappa$ , the wavelength systematically increases with distance from the source. This behavior is attributable to the divergence of the “characteristics” in (29) (see Appendix A). For  $\kappa = 0.65$ , the flow depth attains a new level that remains essentially constant beyond three length scales. This is the upper  $\kappa$  value that represents a stable but time-dependent flow regime. This  $\kappa$  value can vary somewhat, depending on our choice of input parameters. For  $\kappa = 3$ , any perturbations in the source boundary conditions grow systematically without bound, equivalent to a regime of instability in the flow conditions. Surface waves analogous to roll-waves might be produced in this regime, but they are not directly related to any pulsations in the boundary conditions at the source. These conclusions hold for other values of  $P^*$  and times of the same order of magnitude as those considered in Figure 4.

[46] Figure 5 provides a series of snapshots of the perturbed flow surface for the case of  $\kappa = 0.65$  at dimensionless times  $t^*$  of 1, 3, and 5. For visualization purposes, the curves for the different times have been vertically offset. An observer stationed within one length scale of the source would see rather irregular, chaotic behavior in the shape of the upper surface. Due to the time-dependent changes in the amplitude and wavelength, it would be difficult to associate this with a simple sinusoidal oscillation in the flow thickness at the source. Conversely, an observer beyond  $\sim 3$  length scales from the source would simply see a more or less constant perturbation above the flow thickness of the reference solution and would also have difficulty associating the flow profile with the type of disturbances at the source.

[47] Figure 6 shows what happens to the perturbed flow surface when the period  $P^*$  is small compared to 1. In physical dimensions, this means that the period of the disturbances at the source is small compared to the decay constant of the boundary condition. In Figure 6,  $P^* = 0.05$

and the  $\kappa$  values remain the same as in Figure 4. The overall behaviors are the same as in Figure 4 except that now the waveforms for all  $\kappa$  values retain the oscillations from the source. The contrast between Figures 4 and 6 provides a potentially important diagnostic of unobserved emplacement conditions.

## 7. Applications to Catastrophic Mass Flows on Mars

[48] We now explore the implications of our results with the assumption that the Martian transverse ridged deposits in the plains to the northwest of Arsia and Pavonis Montes are the result of mass flows initiated on the upper flanks of the volcanoes. Our approach is to input reasonable parameters into the key equations of our perturbation analysis, and to see whether surface waves leading to transverse ridges would likely be generated. Thus this is an extension of the steady state analysis presented in section 3 for the case of a time-dependent catastrophic release. Table 5 summarizes our input parameters and computations, which are explained below.

[49] A reasonable estimate of  $u_0$  for the Martian deposits can be obtained by correcting a terrestrial velocity for the lower Martian gravity and different slopes. From (12),

$$u_{0\_mars} = u_{0\_earth} \sqrt{\frac{g_{mars} h_{0\_mars} \sin \theta_{mars} C_{earth}}{g_{earth} h_{0\_earth} \sin \theta_{earth} C_{mars}}}. \quad (31)$$

[50] The upper flanks of Arsia and Pavonis Mons, where the ridged deposits presumably originated, have slopes approaching  $3^\circ$ . Using this value for  $\theta_{mars}$ , and holding  $h_0$  and  $C$  constant, a typical terrestrial flow with  $u_0 = 45$  m/s and  $\theta_{earth} = 6^\circ$  would scale to a Martian  $u_0$  of  $\sim 20$  m/s. Critically, this suite of parameters yields epsilon values sufficiently small to enable us to apply our analysis. Other values of slopes and velocities are certainly plausible, but

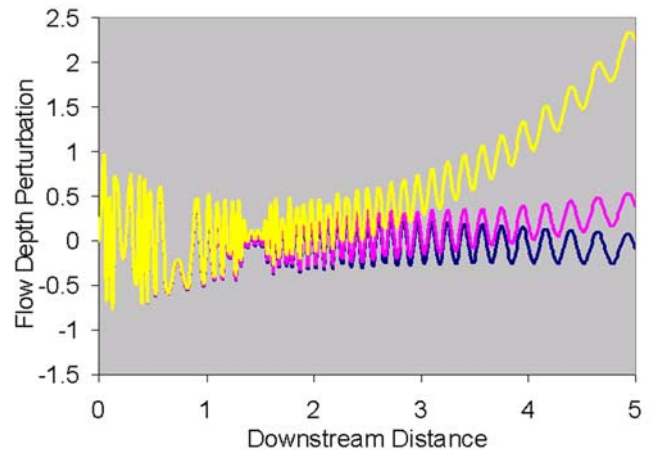


**Figure 6.** Plot of flow depth perturbation ( $\eta$ ) as a function of downstream distance ( $x^*$ ) for  $P^* = 0.05$ . Both axes are dimensionless. Three different  $\kappa$  values are shown: 0.05 (bottom curve), 0.65 (middle curve), and 3 (top curve). Oscillations in flow depth at the source persist downstream for all  $\kappa$  values, even for the unstable  $\kappa = 3$  case that grows without bound. Note the irregular appearance of the surface waves.

**Table 5.** Perturbation Analysis of Arsia and Pavonis Montes Ridged Flows

	Short Duration			Long Duration		
	1	2	3	4	5	6
	<i>Inputs</i>					
$T$ , s	2400	2400	2400	18000	18000	18000
$u_0$ , m/s	20	20	20	20	20	20
$\theta$	3	3	3	3	3	3
$g$ , m/s <sup>2</sup>	3.74	3.74	3.74	3.74	3.74	3.74
$\kappa$	0.05	0.65	3	0.05	0.65	3
	<i>Computations</i>					
$\Gamma$	1108.8	1108.8	1108.8	8316	8316	8316
$L$ , km (from 15)	33.3	33.3	33.3	249.5	249.5	249.5
$\varepsilon$ (from 22)	0.092	0.092	0.092	0.012	0.012	0.012
$C$ (from 23)	0.004	0.051	0.236	0.004	0.051	0.236

our choices are constrained by our requirement that  $\varepsilon$  be small compared to unity.

[51] To apply the results from the time-dependent analysis (sections 5 and 6) to these Martian deposits, we must obtain some estimate of the time constant  $\Gamma$ . This can be estimated from  $T$ , the total duration of time required for all the mass to flow from the nominal source location at  $x = 0$ . The boundary condition we have used technically requires an infinite amount of time for the flow depth at the source to reach zero. For estimation purposes, we let the flow depth decay to 0.1 of its initial value to obtain a relationship between  $\Gamma$  and  $T$ . Methods of estimating  $\Gamma$  for terrestrial applications are given by *Glaze et al.* [2002] and *Fagents and Baloga* [2004]. Here we use  $\Gamma = 0.462 T$ .

[52] Accounts of the Elm landslide indicate that the release of mass occurred over  $T \sim 20$  minutes [*Heim*, 1882, 1932]. The Martian deposits (and presumably their source areas) are significantly larger than their Elm counterparts, and their emplacement velocities are likely lower. Thus a greater  $T$  is presumed for the Martian deposits, but how much greater is difficult to constrain. Here, we consider  $T$  values of 40 minutes (2400 s) and 5 hours (18000 s). For each  $T$ , we consider three values of  $\kappa$  (0.05, 0.65 and 3), consistent with those used in Figure 4. The length scale  $L$ , dimensionless parameter  $\varepsilon$  and flow resistance coefficient  $C$  are computed directly from (15), (22) and (23), respectively (Table 5). For both choices of  $T$ ,  $\varepsilon$  is sufficiently small such that quadratic terms can be ignored, as required by this analysis.

[53] If the deposits originated as landslides or lahars from the flanks of the volcano, then their total transit distances were likely on the order of several hundred km. Given these great distances, Table 5 and Figure 4 provide implications about a dynamic origin for the transverse ridged deposits. For short timescales (Table 5, columns 1–3), the length scale  $L$  is only  $\sim 33$  km. For  $\kappa \leq 0.65$ , any waves associated with pulses or irregularities in the source conditions would have decayed away over the large number of length scales traversed by these flows (Figure 4). Thus the parameters shown in the first two columns could not have produced the ridged deposits. This is also consistent with the low derived  $C$  values, which tend to represent rather fluid mass flows in terrestrial settings [*Baloga et al.*, 1995; *Bulmer et al.*, 2002a; *Glaze et al.*, 2002].

[54] However, the unstable short-duration case denoted by  $\kappa = 3$  (column 3) is a viable candidate. As the insta-

bilities grow, one would expect some analog of roll waves to form. In view of (13) and (14), the steady state that produces roll waves is approached in the limit as  $\Gamma$  becomes large. If the roll-wave analogs for the time-dependent reference solution are indeed the ultimate cause of the ridged deposits, then they are not associated with any pulses or irregularities in the boundary conditions at the source. Moreover, the implied  $C$  value is representative of a dense debris flow or lahar that would be capable of retaining surface structures in the final stage of emplacement. Of course, it is also possible that the ridges were formed by many separate and unrelated mass flow events. Our analysis is not capable of discriminating this type of origin.

[55] A different set of scenarios follows for a long duration of catastrophic release (Table 5, columns 4–6). Now the length scale is an order of magnitude larger, comparable to the extent of the deposits. Any waves generated in the source region must be considered as admissible flow regimes. Even for the unstable case ( $\kappa = 3$ ; column 6), there is not sufficient distance for the instability to manifest itself as fully developed traveling waves. *Jeffreys* [1925] and *Dressler* [1949] both noted the importance of having sufficient runout distances to observe fully developed surface waves. This is almost certainly one of the reasons why wave-like structures and ridges are always observed in catastrophic terrestrial mass flows. Interestingly, the spacing and amplitudes shown in the first few length scales of Figure 4 are reminiscent of the Martian deposits. Although all the cases in columns 4–6 are admissible, the first two  $C$  values typify the more fluid end of mass flows. Consequently, additional processes would have to be conjectured that would allow the deposits to be preserved. As in the short-duration case, the higher  $C$  value associated with  $\kappa = 3$  (column 6) would be most likely to retain wave structures on the deposit surface.

[56] The above discussion assumes similar flow thicknesses for Martian and terrestrial flows. However, the greater extent of the Martian deposits might suggest a greater flow thickness. If we instead assume the Martian flow was twice as thick as the hypothetical terrestrial flow considered above, the Martian  $u_0$  becomes 28 m/s. The corresponding  $L$  values are 47 km and 349 km for the short- and long-duration cases, respectively. All the conclusions above still hold for these thicker flows and, critically,  $\varepsilon$  remains small.

[57] Finally, we note that our method of analysis limits us to the investigation of surface wave structures arising from mass flows with modest velocities (a few tens of m/s) and rather long durations of mass release (tens of minutes or greater). There is little doubt that instabilities and some form of wave structures would arise from faster velocities and shorter durations. However, our ability to investigate such flow regimes is limited by the requirement of the perturbation method that  $\varepsilon$  must be sufficiently small to make terms of  $O(\varepsilon^2)$  negligible. We expect higher-order waves to produce an even richer variety of surface manifestations but reserve such an analysis for future investigations.

## 8. Discussion

[58] When the thickness of a mass flow at the source starts at a relative maximum then decays monotonically with time, there are a host of possible manifestations on the

longitudinal profile of the flow during transit. In general, inertia will tend to destabilize the thickness profile whereas the smoothing influence of pressure will tend to stabilize it.

[59] We have characterized these influences by two dimensionless parameters. The first parameter,  $\varepsilon$ , must be small compared to unity in order to perform our analysis. It depends fundamentally on the initial velocity at the onset of the mass flow and the time constant of the decay (plus gravity and slope). The second parameter,  $\kappa$ , depends on the slope and flow resistance coefficient,  $C$ ;  $\kappa$  ranges from zero to infinity. For  $\kappa$  values sufficiently large (i.e., flows with large flow resistance coefficients or gentle slopes), perturbations in the source depth will grow without bound downstream. This thickening during flow advance is analogous to the classical instability of a uniform steady state on a constant inclined plane. It is well known that roll waves can form when the steady state becomes unstable. For  $\kappa \cong 3$  or greater, we conjecture that surface waves analogous to roll waves form downstream with time-dependent source conditions. We make this conjecture because our time-dependent depth and velocity reference solutions reduce to the steady state as the time constant of boundary conditions becomes infinite. Reminiscent of the early roll wave observations and experiments approximately a century ago, we find that the regime of instability requires long runout distances of many spatial length scales.

[60] We have also investigated the propagation of small disturbances in the thickness at the source of the mass flow. For sinusoidal perturbations, what happens to the surface profile downstream depends critically on the relative values of the oscillation period at the source and the time constant of the decaying boundary condition. When the oscillation period is comparable to the decay constant of the boundary condition, any type of oscillation or perturbation decays downstream. This result holds whether the perturbations remain small or grow without bound (Figure 4). In other words, all connection to the details of the catastrophic release at the source becomes lost downstream. However, when the period of the disturbance at the source is small, the wave structure is preserved at all distances downstream, even in the unstable regime (Figure 6).

[61] Whether the flow regime is stable or unstable, perturbations in the depth at the source become immediately distorted over the first few length scales. Regularly spaced, constant maximum amplitude waves change as they propagate downstream: the wavelength systematically increases and the peak amplitude decays. It would be difficult, if not impossible, for a downstream observer to infer that the irregular, seemingly chaotic profiles were produced by simple sine waves at the source. Surface waveforms with complex amplitudes reminiscent of deposits at Chaos Jumbles and spacings reminiscent of the ridged deposits off the flanks of Tharsis volcanoes are readily produced by small periodic disturbances in the time-dependent boundary conditions.

[62] We have not attempted to argue convincingly that the extensive ridged deposits off the flanks of Arsia and Pavonis Montes are the result of catastrophic mass flows from the summits. We merely point out that the existence of more or less regular ridges can be a natural consequence of the flow dynamics and the time-dependent character of the release of material. Thus a mass flow origin for these

deposits remains a viable possibility that might be reexamined by others.

[63] If the ridged deposits did indeed result from catastrophic landslides, debris flows or lahars, then the existence of the remnants of surface waves engenders new inferences about the emplacement conditions. In one scenario, we assumed a plausible mass release time (40 min) and initial flow velocity (20 m/s) by extrapolating terrestrial experience. For regular disturbances at the source on the order of the release time, we found the only way to produce waves would be through an instability that leads to a time-dependent analog of steady state roll waves. This results in an inferred flow resistance coefficient comparable to that of dense mass flows on Earth. For more fluid materials (e.g., sediment-laden water flows), regular or irregular variations in the source conditions would be damped out well before the mass flows reach the vicinity of their final extent.

[64] For such massive and extensive deposits that are well beyond terrestrial experience, it is certainly plausible that the release time could be much longer than 40 minutes. Thus we explored a second scenario with an increased release time of 5 hours. We found that all regular or irregular perturbations in the flow depth at the source would be preserved over the extent of the flow path, regardless of whether or not the flow is stable. The implied rheologies range from those of dense landslides, dense debris flows or lahars to those associated with sediment-laden and hyperconcentrated water flows. Additional arguments and modeling would have to be undertaken for the relatively dilute cases to explain how the solid deposits remain and what happened to the water. Finally, we investigated the possibility that the extensive Martian flow deposits had greater flow thicknesses than the significantly smaller terrestrial analogs. The same conclusions still hold for both the short- and long-duration scenarios.

## 9. Conclusions

[65] We have shown that a regular pattern of transverse ridges can form on the surfaces of catastrophic mass flow deposits as a natural consequence of the flow dynamics and the time-dependent character of the release of material. These surface waves can result either from a flow instability or from irregularities or pulses in the release of material at the source. By extending classic fluid dynamic stability criteria to the time-dependent case, we show that flow instabilities known to lead to roll waves seem likely for the mass flow deposits studied on Earth and Mars. Although we have not argued that the extensive ridged deposits off the flanks of Arsia and Pavonis Montes are the result of catastrophic mass flows, a mass flow origin for these deposits remains a viable possibility that might be reexamined by others.

[66] The remnants of waves on the surface of mass flow deposits provide a new and independent constraint on the dynamics and the rheologic character of the flow during transit. There are of course shortcomings in the level of analysis presented here. On the theoretical side, we do not understand at present what happens to a surface wave structure on a dense mass flow during the very final stage of emplacement as overall flow advance ceases and intergranular forces quench topographic gradients on the flow

surface. New empirical constants would be required that could only be derived from laboratory study or field experiments. Nor do we understand the structure of roll wave analogs for time-dependent boundary conditions. It is likely that the details of the thickness profile evolution depend on a host of factors related to the release itself (e.g., whether it is initiated from the front and progresses upslope, or whether a broad source area is activated simultaneously). Finally, slope changes and irregular topographic variations certainly play an important role as they directly influence flow inertia and the topographic gradient of the flowing surface. These are all tractable issues whose investigation is warranted by the promise of new diagnostics of the unobserved emplacement conditions that produced transverse waves on mass flows on the Earth and Mars.

## Appendix A

[67] Here we provide the details of the perturbation method used in the text. Volume and momentum conservation are given by

$$\frac{\partial h}{\partial t} + \frac{\partial}{\partial x}(hu) = 0 \quad (\text{A1})$$

and

$$\frac{\partial u}{\partial t} + u \frac{\partial u}{\partial x} = g \sin \theta - Cu^2/h - g \cos \theta \frac{\partial h}{\partial x}. \quad (\text{A2})$$

[68] The time-dependent reference solution is found by ignoring the inertial and pressure terms in (A2) and solving (A1) and (A2) subject to the boundary conditions

$$h(x=0, t) = \frac{h_o}{(1+t/\Gamma)^2} \quad (\text{A3})$$

and

$$u(x=0, t) = \frac{u_o}{(1+t/\Gamma)}, \quad (\text{A4})$$

where

$$u_o = \sqrt{\frac{gh_o \sin \theta}{C}}. \quad (\text{A5})$$

[69] The reference solutions are given [e.g., Glaze *et al.*, 2002; Fagents and Baloga, 2004] by

$$h_r(x, t) = h_o \left( \frac{1+x/L}{1+t/\Gamma} \right)^2 \quad (\text{A6})$$

and

$$u_r(x, t) = u_o \left( \frac{1+x/L}{1+t/\Gamma} \right), \quad (\text{A7})$$

where

$$L = \frac{3\Gamma u_o}{2}. \quad (\text{A8})$$

[70] To facilitate the analysis, we make the volume and momentum conservation equations (A1) and (A2), the boundary conditions (A3) and (A4) and the reference solutions (A6) and (A7) all dimensionless using the natural scaling factors

$$h = h_o h^*, \quad (\text{A9})$$

$$x = Lx^*, \quad (\text{A10})$$

$$t = \Gamma t^*, \quad (\text{A11})$$

$$u = u_o u^*, \quad (\text{A12})$$

where asterisks denote dimensionless terms. With these scalings, the boundary conditions at the source become

$$h^*(x^*=0, t^*) = \frac{1}{(1+t^*)^2} \quad (\text{A13})$$

and

$$u^*(x^*=0, t^*) = \frac{1}{1+t^*}. \quad (\text{A14})$$

[71] Similarly, the reference solutions take the dimensionless forms

$$h_r^*(x^*, t^*) = \left( \frac{1+x^*}{1+t^*} \right)^2 \quad (\text{A15})$$

and

$$u_r^*(x^*, t^*) = \frac{1+x^*}{1+t^*}. \quad (\text{A16})$$

[72] The new forms of volume and momentum conservation are

$$\frac{\partial h^*}{\partial t^*} + \frac{2}{3} \left( h^* \frac{\partial u^*}{\partial x^*} + u^* \frac{\partial h^*}{\partial x^*} \right) = 0 \quad (\text{A17})$$

and

$$\underbrace{\frac{1}{\Gamma} \sqrt{\frac{h_o}{Cg \sin \theta}}}_{\text{prefactor of inertial terms}} \left( \frac{\partial u^*}{\partial t^*} + \frac{2}{3} u^* \frac{\partial u^*}{\partial x^*} \right) = 1 - \frac{u^{*2}}{h^*} - \underbrace{\frac{2h_o \cot \theta}{3\Gamma} \sqrt{\frac{C}{gh_o \sin \theta}}}_{\text{prefactor of pressure}} \frac{\partial h^*}{\partial x^*}. \quad (\text{A18})$$

[73] Our interest in determining the influence of inertial effects on the reference solution makes it natural to define the prefactor of the inertial term as

$$\varepsilon = \frac{1}{\Gamma} \sqrt{\frac{h_o}{Cg \sin \theta}} = \frac{u_o}{\Gamma g \sin \theta} = \frac{3u_o^2}{2gL \sin \theta} \quad (\text{A19})$$

With the perturbation method used below, we will consider only cases that make this constant small compared to unity.

[74] We also define a second dimensionless parameter,

$$\kappa = \frac{2C \cot \theta}{3}, \quad (\text{A20})$$

and thus we can rewrite (A18) as

$$\varepsilon \left( \frac{\partial u^*}{\partial t^*} + \frac{2}{3} u^* \frac{\partial u^*}{\partial x^*} + \kappa \frac{\partial h^*}{\partial x^*} \right) = 1 - \frac{u^{*2}}{h^*}. \quad (\text{A21})$$

Equations (A17) and (A21) have the identical physical content as (A1) and (A2). We have simply made a judicious choice of scalings to simplify the appearance of the equations and facilitate the application of the perturbation method.

[75] We now consider perturbation expansions in the flow depth and velocity:

$$h^* = h_R^* + \varepsilon \eta + O(\varepsilon^2), \quad (\text{A22})$$

$$u^* = u_R^* + \varepsilon \xi + O(\varepsilon^2), \quad (\text{A23})$$

where  $O(\varepsilon^2)$  indicates terms quadratic or higher in  $\varepsilon$ . Thus the flow depth and velocity are considered to be those given essentially by the reference solutions plus small corrections specified by two functions  $\xi(x, t)$  and  $\eta(x, t)$  that must be determined.

[76] We first find the two linear equations that  $\xi$  and  $\eta$  must satisfy when  $\varepsilon$  is small enough to make any quadratic terms negligible. Plugging (A22) and (A23) into the volume conservation equation (A17) and disregarding terms quadratic in  $\varepsilon$ :

$$\left( \frac{\partial h_R^*}{\partial t^*} + \varepsilon \frac{\partial \eta}{\partial t^*} \right) + \frac{2}{3} \left( h_R^* \frac{\partial u_R^*}{\partial x^*} + h_R^* \varepsilon \frac{\partial \xi}{\partial x^*} + \varepsilon \eta \frac{\partial u_R^*}{\partial x^*} + u_R^* \frac{\partial h_R^*}{\partial x^*} + u_R^* \varepsilon \frac{\partial \eta}{\partial x^*} + \varepsilon \xi \frac{\partial h_R^*}{\partial x^*} \right) = 0, \quad (\text{A24})$$

[77] The next key step in the perturbation scheme is to set the terms to zeroth and first order in  $\varepsilon$  in (A24) each equal to zero. This gives two separate equations shown in (A25) and (A26), respectively:

$$\varepsilon^0 \quad \frac{\partial h_R^*}{\partial t^*} + \frac{2}{3} \left( h_R^* \frac{\partial u_R^*}{\partial x^*} + u_R^* \frac{\partial h_R^*}{\partial x^*} \right) = 0, \quad (\text{A25})$$

$$\varepsilon^1 \quad \left( \frac{\partial \eta}{\partial t^*} \right) + \frac{2}{3} \left( h_R^* \frac{\partial \xi}{\partial x^*} + \eta \frac{\partial u_R^*}{\partial x^*} + u_R^* \frac{\partial \eta}{\partial x^*} + \xi \frac{\partial h_R^*}{\partial x^*} \right) = 0. \quad (\text{A26})$$

[78] A ‘‘reference solution,’’ by definition, must satisfy (A25). The dimensionless time-dependent reference solutions (A15) and (A16) can be shown to satisfy (A25) simply by substitution. Obviously, the constant steady state solu-

tions for a uniform flow on a constant inclined plane satisfy (A25) as well.

[79] Equation (A26) is the first equation governing the perturbations  $\xi$  and  $\eta$ . It shows that the reference solutions  $h_R$  and  $u_R$  introduce both spatial and time variability in the coefficients of this linear partial differential equation.

[80] Substituting the perturbations (A22) and (A23) into the momentum equation (A21) gives

$$\varepsilon \left( \frac{\partial u_R^*}{\partial t^*} + \varepsilon \frac{\partial \xi}{\partial t^*} + \frac{2}{3} u_R^* \frac{\partial u_R^*}{\partial x^*} + \frac{2}{3} u_R^* \varepsilon \frac{\partial \xi}{\partial x^*} + \frac{2}{3} \varepsilon \xi \frac{\partial u_R^*}{\partial x^*} + \kappa \frac{\partial h_R^*}{\partial x^*} + \varepsilon \kappa \frac{\partial \eta}{\partial x^*} \right) = 1 - \frac{u_R^{*2}}{h_R^*} + \frac{u_R^{*2} \varepsilon \eta}{h_R^{*2}} - \frac{2u_R^* \varepsilon \xi}{h_R^*}, \quad (\text{A27})$$

where a Taylor expansion has been used on the right-hand side of (A21). Collecting the terms to zeroth order in  $\varepsilon$ , we have

$$\varepsilon^0 \quad 0 = 1 - \frac{u_R^{*2}}{h_R^*} \quad (\text{A28})$$

regardless of whether the reference solution is time-dependent or not.

[81] When terms to first order in  $\varepsilon$  are collected from (A27), we have

$$\varepsilon^1 \quad \left( \frac{2u_R^*}{h_R^*} \right) \xi - \frac{u_R^{*2}}{h_R^{*2}} \eta + \left( \frac{2}{3} u_R^* \frac{\partial u_R^*}{\partial x^*} + \kappa \frac{\partial h_R^*}{\partial x^*} + \frac{\partial u_R^*}{\partial t^*} \right) = 0. \quad (\text{A29})$$

Equation (A29) is the second equation linking the perturbations  $\xi$  and  $\eta$ . It is particularly fortunate here that this equation has no derivatives of  $\xi$  and  $\eta$ . The derivatives all act on the reference solution and can thus be readily computed. Unlike (A26), there is only an algebraic relationship to solve in (A29), not a partial differential equation.

[82] We obtain the equation governing the evolution of the perturbations  $\xi$  and  $\eta$  by first solving (A29) for  $\xi$  in terms of  $\eta$ , then inputting that result into (A26). This results in a single partial differential equation in only one unknown ( $\eta$ ). After taking the derivatives of the reference solutions as indicated in (A29), we have after some algebra

$$\xi = \frac{\eta}{2} \frac{(1+t^*)}{(1+x^*)} + \left( \frac{1}{6} - \kappa \right) \frac{(1+x^*)^2}{(1+t^*)^3}. \quad (\text{A30})$$

Substituting (A30) into (A26) yields

$$\frac{\partial \eta}{\partial t^*} + \frac{(1+x^*)}{(1+t^*)} \frac{\partial \eta}{\partial x^*} + \frac{\eta}{(1+t^*)} + \left( \frac{4}{9} - \frac{8}{3} \kappa \right) \frac{(1+x^*)^3}{(1+t^*)^5} = 0. \quad (\text{A31})$$

Equation (A31) is the primary result of the perturbation approach. It is a linear inhomogeneous first-order partial differential equation for the perturbation of the flow depth. This equation can be solved in the general case for either initial or boundary conditions on the flow depth using well-known methods. Once  $\eta$  is known explicitly as a function of  $x^*$  and  $t^*$ , (A30) can be used to compute the perturbation in the flow velocity,  $\xi$ , as an explicit function of  $x^*$  and  $t^*$ .

[83] We now find the general solution of (A31) using the method of characteristics [Whitham, 1974; Zachmanoglou and Thoe, 1986]. Equation (A31) is equivalent to the system of ordinary differential equations:

$$dt^* = \frac{(1+t^*)}{(1+x^*)} dx^* = \frac{d\eta}{\frac{-\eta}{(1+t^*)} + \left(-\frac{4}{9} + \frac{8}{3}\kappa\right) \frac{(1+x^*)^3}{(1+t^*)^5}}. \quad (\text{A32})$$

[84] To obtain the general solution for a boundary value problem, one must prescribe the time-dependent behavior of  $\eta(x^*, t^*)$  at  $x^* = 0$  by a function  $\eta(x^* = 0, t^*) = \eta_0(t^*)$ . Physically, this means one must specify how the perturbation in the flow depth at the source behaves as a function of time. Following a common notation used in the method of characteristics, we use the symbol  $\tau$  to parameterize the values of time for  $\eta(x^*, t^*)$  when  $x^* = 0$ . The boundary condition is written as  $\eta_0(\tau)$ , where the form of  $\tau = \tau(x^*, t^*)$  is to be determined by integrating the left-hand equality of (A32).

[85] To obtain a general solution, we must obtain solutions to two of the ordinary differential equations given by (A32). Integrating the left-hand equality gives

$$1 + t^* = (1 + x^*)e^c, \quad (\text{A33})$$

where  $c$  is the constant of integration. Because  $\tau = t^*$  when  $x^* = 0$ , (A33) reduces to

$$1 + t^* = (1 + x^*)(1 + \tau)$$

or

$$\tau = \tau(x^*, t^*) = \frac{1 + t^*}{1 + x^*} - 1. \quad (\text{A34})$$

[86] Physically, we are interested only in the admissible region for the solution:

$$t^* \geq x^* \geq 0. \quad (\text{A35})$$

To find the second integral necessary for a general solution of (A31), the right-hand equality of (A32) can be put in the form

$$\frac{d\eta}{dx^*} = \frac{-\eta}{(1+x^*)} - \left(\frac{4}{9} - \frac{8}{3}\kappa\right) \frac{(1+x^*)^2}{(1+t^*)^4}. \quad (\text{A36})$$

Now, according to the method of characteristics, we replace the times appearing in (A36) in terms of  $\tau$  using (A34) and integrate both sides:

$$\begin{aligned} \int_0^{x^*} \frac{d}{dx^*} [(1+x^*)\eta] dx^* &= -\left(\frac{4}{9} - \frac{8}{3}\kappa\right) \frac{1}{(1+\tau^*)^4} \int_0^{x^*} \frac{1}{1+x^*} dx^*, \\ (1+x^*)\eta|_0^{x^*} &= -\left(\frac{4}{9} - \frac{8}{3}\kappa\right) \frac{\ln(1+x^*)|_0^{x^*}}{(1+\tau^*)^4}, \\ (1+x^*)\eta - \eta_0 &= -\left(\frac{4}{9} - \frac{8}{3}\kappa\right) \frac{\ln(1+x^*)}{(1+\tau^*)^4}. \end{aligned} \quad (\text{A37})$$

We now have the general solution of the boundary value problem for  $\eta$ ,

$$\eta(x^*, t^*) = \frac{\eta_0(\tau)}{(1+x^*)} - \left(\frac{4}{9} - \frac{8}{3}\kappa\right) \frac{(1+x^*)^3 \ln(1+x^*)}{(1+t^*)^4}, \quad (\text{A38})$$

in terms of the arbitrary function  $\eta(x^* = 0, t^*) = \eta_0(t^*)$ . The solution shown in (A38) is the main result of the mathematical analysis and forms the basis for all the results discussed in the text.

[87] **Acknowledgments.** James Zimbelman provided a thorough, useful review of this manuscript. Mark Bulmer and Julio Friedmann shared images, related data, and many insights regarding terrestrial and Martian landslide deposits. This research was supported by NAG5-12682. This paper is HIGP publication 1372 and SOEST publication 6542.

## References

- Baloga, S. M., P. D. Spudis, and J. E. Guest (1995), The dynamics of rapidly emplaced terrestrial lava flows and implications for planetary volcanism, *J. Geophys. Res.*, *100*, 24,509–24,519.
- Bulmer, M. H., O. S. Barnouin-Jha, M. N. Peitersen, and M. Bourke (2002a), An empirical approach to studying debris flows: Implications for planetary modeling studies, *J. Geophys. Res.*, *107*(E5), 5033, doi:10.1029/2001JE001531.
- Bulmer, M. H., L. S. Glaze, O. S. Barnouin-Jha, W. Murphy, and G. Neumann (2002b), Modeling mass movements on Mars, *Eos Trans. AGU*, *83*(19), Spring Meet. Suppl., Abstract P32B-03.
- Bulmer, M. H., L. S. Glaze, O. S. Barnouin-Jha, W. Murphy, and G. Neumann (2002c), Modelling mass movements for planetary studies, *Lunar Planet. Sci.*, *XXXIII*, abstract 1533.
- Bulmer, M. H., L. S. Glaze, K. M. Shockey, O. S. Barnouin-Jha, and W. Murphy (2003), Insights into the emplacement of rock avalanches on Mars, *Lunar Planet. Sci.*, *XXXIV*, abstract 1225.
- Carver, S., D. Sear, and E. Valentine (1994), An observation of roll waves in a supra-glacial meltwater channel, Harlech Gletscher, East Greenland, *J. Geol.*, *134*, 177–180.
- Chow, V. T. (1973), *Open-Channel Hydraulics*, 680 pp., McGraw-Hill, New York.
- Cornish, V. (1910), *Waves of the Sea and Other Waves*, CRC Press, Boca Raton, Fla.
- Dressler, R. F. (1949), Mathematical solution of the problem of roll waves in inclined open channel, *Commun. Pure Appl. Math.*, *2*, 149–194.
- Eppler, D. B., J. H. Fink, and R. Fletcher (1987), Rheologic properties and kinematics of emplacement of the Chaos Jumbles rockfall avalanche, Lassen Volcanic National Park, California, *J. Geophys. Res.*, *92*, 3623–3633.
- Fagents, S. A., and S. M. Baloga (2004), Calculation of lahar transit times using digital elevation data, *J. Volcanol. Geotherm.*, *139*, 135–146, doi:10.1016/j.jvolgeores.2004.06.013.
- Glaze, L. S., S. M. Baloga, and O. S. Barnouin-Jha (2002), Rheologic inferences from high water marks of debris flows, *Geophys. Res. Lett.*, *29*(8), 1208, doi:10.1029/2002GL014757.
- Head, J. W., and D. R. Marchant (2003), Cold-based mountain glaciers on Mars: Western Arsia Mons, *Geology*, *31*(7), 641–644.
- Heim, A. (1882), Der Bergsturz von Elm, *Z. Dtsch. Geol. Ges.*, *34*, 74–115.
- Heim, A. (1932), *Bergsturz und Menschenleben*, 476 pp., Fretz and Wasmuth, Zurich.
- Iverson, R. M. (1997), The physics of debris flows, *Rev. Geophys.*, *35*, 245–296.
- Jeffreys, H. J. (1925), The flow of water in an inclined channel of rectangular section, *Philos. Mag.*, *49*(6), 793–807.
- Kreyszig, E. (1988), *Advanced Engineering Mathematics*, John Wiley, Hoboken, N. J.
- Lipman, P. W., and N. G. Banks (1987), Aa flow dynamics, Mauna Loa 1984, in *Volcanism in Hawaii*, edited by R. W. Decker, T. L. Wright, and P. H. Stauffer, *U.S. Geol. Surv. Prof. Pap.*, *1350*, 1527–1567.
- Moore, H. J. (1987), Preliminary estimates of the rheological properties of 1984 Mauna Loa lava, in *Volcanism in Hawaii*, edited by R. W. Decker, T. L. Wright, and P. H. Stauffer, *U.S. Geol. Surv. Prof. Pap.*, *1350*, 1569–1588.
- Morris, A., P. J. Mougini-Mark, and S. Baloga (2003), Did glaciers exist recently on the Tharsis Montes?, *Eos Trans. AGU*, *84*(46), Fall Meet. Suppl., Abstract P32C-08.

- Shean, D. E., and J. W. Head (2003), Pavonis Mons fan-shaped deposits: A cold-based glacial model, *Lunar Planet. Sci.*, XXXIV, abstract 1153.
- Shreve, R. L. (1968), The Blackhawk landslide, *Geol. Soc. Am. Spec. Pap.*, 108, 47 pp.
- Takahashi, T. (1980), Debris flow on prismatic open channel, *J. Hydraul. Div. Am. Soc. Civ. Eng.*, 106, 381–396.
- Townson, J. M. (1991), *Free Surface Hydraulics*, 228 pp., CRC Press, Boca Raton, Fla.
- Weir, G. J. (1982), Kinematic wave theory for Ruapehu lahars, *N. Z. J. Sci.*, 25, 197–203.
- Whitham, G. B. (1974), *Linear and Nonlinear Waves*, 636 pp., Wiley-Interscience, Hoboken, N. J.
- Zachmanoglou, E. C., and D. W. Thoe (1986), *Introduction to Partial Differential Equations With Applications*, 405 pp., Dover, Mineola, N. Y.
- Zauderer, E. (1983), *Partial Differential Equations of Applied Mathematics*, 779 pp., Wiley-Interscience, Hoboken, N. J.
- 
- S. M. Baloga, Proxemy Research, 14300 Gallant Fox Lane, Bowie, MD 20715, USA.
- B. C. Bruno, Hawai'i Institute of Geophysics and Planetology, University of Hawai'i, 2525 Correa Road, Honolulu, HI 96822, USA. (barb@hawaii.edu)